

# On the Response of a Freely Vibrating Thick Elliptic Cylinder of Low Mass Ratio

K. Sourav and S. Sen<sup>†</sup>

*Department of Mechanical Engineering, Indian Institute of Technology (ISM) Dhanbad  
Dhanbad - 826004, Jharkhand, India*

<sup>†</sup>Corresponding Author Email: [subhankars@gmail.com](mailto:subhankars@gmail.com)

(Received June 16, 2016; accepted January 21, 2017)

## ABSTRACT

Two-dimensional space-time finite-element simulations are carried out to study the free vibrations of a rigid elliptic cylinder of aspect ratio 1.11 and low non-dimensional mass of unity. Undamped transverse-only as well as two-degrees-of-freedom oscillations are considered. The effect of damping is investigated on transverse-only motion. For all three cases, results for cylinder response are presented for  $50 \leq Re \leq 180$ . In the absence of damping, transverse oscillations are mostly periodic except for a very narrow region near the end of lock-in. In contrast, a damping of 0.044 removes quasi-periodicity as well as secondary hysteresis from flow and body motion. For undamped motion, inclusion of in-line oscillations excites high amplitude oscillations, widens the range of synchronization and delays phase shift between lift and cross-stream response. In each case, synchronization between cylinder oscillations and vortex-shedding is 1:1. In addition, drag-lift phase plots are symmetric about mean lift (= 0) line. Thus, symmetrical shedding of two equally strong alternate vortices per oscillation cycle forms 2S, C<sub>NW</sub>(2S) or C(2S) modes. For each case, the lower branch initiates at  $Re = 65$  where the oscillation or shedding frequency is found to be locally maximum.

**Keywords:** Elliptic cylinder; Free vibration; Damping; Quasi-periodic; Single and two-degrees-of-freedom.

## NOMENCLATURE

$AR$	aspect ratio of the ellipse	$U^*$	reduced speed
$B, D$	streamwise and transverse lengths of ellipse	$x, y$	spatial coordinates w.r.t. Cartesian axes
$C_d, C_l$	drag and lift coefficients	$X, Y$	in-line and transverse displacements
$F_N$	reduced natural frequency	<b>Subscripts</b>	
$L_u, L_d$	distance of inlet and exit boundaries	$max$	maximum value
$m^*$	mass ratio	$r.m.s.$	root mean square value
$Re$	Reynolds number	$\rho$	density of the fluid
$St$	Strouhal number	$\sigma$	stress tensor
$t$	time	$\zeta$	damping coefficient
$\mathbf{u}$	velocity vector		

## 1. INTRODUCTION

The free or vortex-induced vibrations (VIV) of a flexibly mounted rigid structure is a vastly emerging research area belonging to fluid-structure interactions (FSI). Experimental and direct numerical simulations of the flow, rigid body vibrations are the two primary approaches for solving

the FSI problems. The numerical treatment is traditionally performed by the partitioned or staggered and simultaneous or monolithic methods. In the former, the fluid and solid media are handled separately while coupling between them is maintained via the dynamic no-slip condition. In contrast, in the monolithic approach, the equations governing the motion of fluid and solid are solved

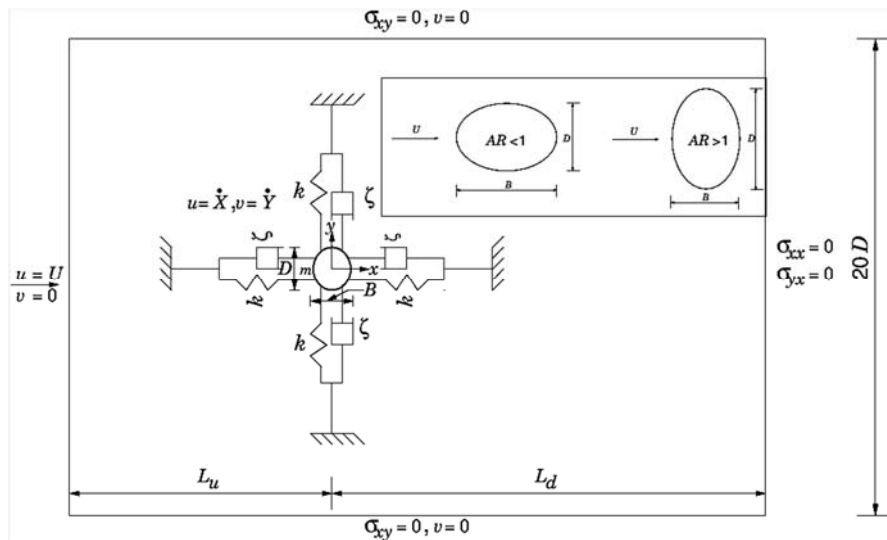


**Fig. 1. Illustration of problem statement for an elastically mounted rigid ellipse undergoing two-degrees-of-freedom free vibrations using 5% blockage. The schematic corresponds to  $tU/D = 0$ . The reference frame as well as outer rectangular boundary are fixed for all times. The inset illustrates the symmetric elliptic cylinder configurations corresponding to  $AR < 1$  and  $> 1$ .**

simultaneously. The current body of work relates to the partitioned formulation. Besides the oscillator cross-section, the non-dimensional oscillator parameters of interest in VIV include mass ratio or relative density ( $m^*$ ), coefficient of structural damping ( $\zeta$ ) and reduced speed ( $U^*$ ) while the Reynolds number ( $Re$ ) is the dimensionless controlling parameter of flow. Mass ratio of the oscillator is the ratio of oscillator mass per unit length ( $m$ ) and mass of displaced fluid ( $m_d$ ).

### 1.1 Earlier Studies

The elliptic cylinder is a canonical geometry that covers a wide range of shapes in the limits of a circle and flat plate. For symmetric elliptic cylinders (angle of incidence =  $0^\circ$  or  $90^\circ$ ), the ratio of lengths of cross-stream projection ( $D$ ) to streamwise projection ( $B$ ) defines its aspect ratio ( $AR = D/B$ ). For zero incidence, the aspect ratio becomes smaller than one. In contrast, for  $90^\circ$  incidence, the value of  $AR$  exceeds one. The inset of Fig. 1 illustrates the definition of  $AR$  for both the cases. While some studies on stationary elliptic cylinders concerning flow (Lugt and Haussling 1974; Sivakumar *et al.* 2007; Sen *et al.* 2012) are available, not much is known on the flow around a translating elliptic cylinder. Jauvtis and Williamson (2004) experimentally demonstrated that the response of a circular cylinder ( $AR = 1$ ) with transverse or  $Y$ -only and simultaneous in-line ( $X$ -) and transverse motion is virtually the same provided  $m^* \geq 6$  and significantly different otherwise. This study establishes the dominant role of  $X$ -motion at low  $m^*$ . By employing the stabilized space-time finite-element formulation of Tezduyar *et al.* (1992 a, b), Sen (2010) studied two degrees-of-freedom (2-DOF or  $X$ - $Y$ ) free vibrations of thick elliptic cylinders with longer axis aligned ( $AR = 0.9$ ) and normal ( $AR = 1.1$ ) to the free-stream. For

$Re = 60-150$ , the cylinders of  $m^* = 10$  were allowed to execute undamped VIV. An increase of the transverse displacement with increasing  $AR$  was observed. Near the fundamental synchronization, the transverse response of a circular cylinder of mass ratio of the order of 10 is about ( $<$ ) 0.6 times its diameter (Khalak and Williamson 1999 at high  $Re$  and Singh and Mittal 2005 at low  $Re$ ; both in lower branch). The concept of branching of cylinder response was introduced by Khalak and Williamson (1996). The maximum response of  $AR = 1.11$  cylinder obtained at  $Re = 83$  by Sen (2010) surpasses the upper limit; the response was found to be about 0.6158 times the length of longer axis ( $D$ ). The study also showed that the maximum transverse response as well as range of lock-in of thick elliptic cylinders overshadows the ones from its circular and square counterparts using identical control parameters for flow and VIV. For  $2000 < Re < 8000$ , Franzini *et al.* (2009) experimentally investigated the transverse oscillations of elliptic cylinders of  $m^* \approx 2.5$ . A detailed numerical study on the effect of  $AR$  on 2-DOF VIV of elliptic cylinders were performed by Navrose *et al.* (2014). The  $AR$  was varied from 0.7 to 1.43 and the range of  $Re$  was 60 to 140. For the entire set of  $AR$ , six distinct regimes of resonance were identified. With rising  $Re$  or  $U^*$ , the sequence of their appearance is – steady state, quasi-periodic (QP) initial branch, periodic initial branch, periodic lower branch, quasi-periodic lower branch and desynchronization. For cylinders of  $AR \geq 1.11$ , Navrose *et al.* (2014) noted in the periodic initial branch, a near wake merging of like sign vortices that differ from conventional C (2S) merging. They introduced the terminology 'C<sub>NW</sub> (2S) mode' to depict the near wake merging. For each  $AR$ , the peak transverse response was found at the periodic lower branch and the peak value continued to rise with increasing  $AR$ .

### 1.2 Objectives of the Current Work

Recently, Sen and Mittal (2015, 2016) reported for a freely vibrating square cylinder with undamped  $X$ - $Y$ -motion, certain fundamental differences in the VIV characteristics for low ( $m^* = 1$ ) and high mass ratios ( $m^* = 5, 10$  and  $20$ ). The earlier studies on undamped VIV concerning circular (Prasanth and Mittal 2008) and elliptic (Navrose *et al.* 2014) cylinders of  $m^* = 10$  suggest that a hysteresis-free regime exists near the onset of lock-in under certain conditions (e.g., low blockage or low  $m^*$ ). However, flow and body motion were hysteretic (secondary) near the closure of lock-in. The choice of  $m^* = 1$  in the present study is motivated by the conclusions of Jauvtis and Williamson (2004) and findings of Prasanth and Mittal (2008) and Navrose *et al.* (2014) for  $m^* = 10 > 6$ . A fundamental question regarding the hysteretic behaviour of oscillators having curved contours therefore relates to conditions that might suppress secondary hysteresis. The motivation behind the current work is derived from following queries: does a secondary hysteresis-free solution exist for oscillating cylinders with curved contours? How does the secondary hysteresis tally with  $\zeta$  or DOF? Is it possible to have solutions completely devoid of hysteresis? To what extent does the  $X$ -motion amplify the  $Y$ -displacement? Efforts are made here to address the aforesaid queries. To understand the role of  $X$ -motion on the undamped response of an elliptic cylinder, a low mass ratio of unity has been used. Results have also been presented for  $m^* = 1$  cylinder for damped ( $\zeta = 0.044$ ) VIV. For all three cases,  $Re$  varies from 50 to 180. The most interesting outcome of this work is the observation of almost or complete disappearance of secondary hysteresis for  $Y$ -only motion of the cylinder.

## 2. METHODOLOGY

### 2.1 Governing Equations

In vector form, the dimensional Navier-Stokes equations of motion governing unsteady incompressible flow of a viscous fluid in a spatial domain  $\Omega_t$  and temporal domain  $(0, T)$  are

$$\nabla \cdot \bar{u} = 0 \tag{1}$$

$$\rho(\partial \bar{u} / \partial t + \bar{u} \cdot \nabla \bar{u}) = \nabla \cdot \bar{\sigma} \tag{2}$$

Here,  $\bar{u} = (u, v)$  and  $\bar{\sigma}$  are the velocity vector and stress tensor, respectively.  $\rho$  is the density of the fluid and  $t$  represents time. Translation of the rigid body is governed by Newton's second law of motion. For an elastically mounted rigid oscillator executing 2-DOF translations, the system of dimensional equations comprising those for in-line and transverse motion are expressed by the following second order ordinary differential equations in time

$$m(\ddot{X}, \ddot{Y}) + c(\dot{X}, \dot{Y}) + k(X, Y) = F_x, F_y \tag{3}$$

where  $c$  and  $k$  are viscous damping and spring stiffness, respectively.  $F_x$  and  $F_y$  are vortex-induced drag and lift forces. Normalization of spatial and

temporal scales are done as  $X^* = \frac{X}{D}$ ,  $Y^* = \frac{Y}{D}$  and

$t^* = \frac{tU}{D}$  where  $U$  is the free-stream speed. The normalized parameters of interest governing the VIV are defined as

$$\zeta = \frac{c}{2\sqrt{km}}, \omega = 2\pi f_N = \sqrt{\frac{k}{m}}, C_d(t) = \frac{F_x(t)}{0.5\rho U^2 D}$$

$$C_l(t) = \frac{F_y(t)}{0.5\rho U^2 D}, m^* = \frac{m}{m_d} \quad \text{where } f_N \text{ is the}$$

dimensional natural frequency of the oscillator. The  $X$ -component of Eq. (3) for an oscillator of arbitrary shape may be simplified as

$$\ddot{X} + 2\zeta\omega\dot{X} + \omega^2 X = \frac{0.5\rho U^2 C_d D}{m^* m_d} \tag{4}$$

For an ellipse with axes  $D$  and  $B$ ,  $m_d = \frac{\pi}{4} DB\rho$  and

$$m^* = \frac{4m}{\rho\pi DB}. \text{ Thus, Eq. (4) reduces to}$$

$$\frac{U^2}{D} \ddot{X} + U4\pi f_N \zeta \dot{X} + 4\pi^2 f_N^2 X^* D = \left(\frac{C_d}{2m^*}\right)\left(\frac{4D}{\pi DB}\right)U^2 \tag{5}$$

Further simplification leads to

$$\ddot{X} + 4\pi \frac{f_N D}{U} \zeta \dot{X} + 4\pi^2 \frac{f_N^2 D^2}{U^2} X^* = \left(\frac{C_d}{2m^*}\right)\left(\frac{4D}{\pi B}\right) \tag{6}$$

The reduced or non-dimensional natural frequency of the oscillator ( $F_N$ ) is obtained by normalizing  $f_N$  by  $D$  and  $U$  to yield  $F_N = f_N D/U$ . Therefore, the final non-dimensional form of the equation of in-line translation of a symmetric ellipse is

$$\ddot{X} + 4\pi F_N \zeta \dot{X} + 4\pi^2 F_N^2 X^* = \left(\frac{2C_d}{\pi m^*}\right)\left(\frac{D}{B}\right) = \left(\frac{2C_d}{\pi m^*}\right)AR \tag{7}$$

Equation (7) is valid for  $AR < 1, = 1$  and  $> 1$ . Similarly, the non-dimensional form of the equation of transverse translation is given by

$$\ddot{Y} + 4\pi F_N \zeta \dot{Y} + 4\pi^2 F_N^2 Y^* = \left(\frac{2C_l}{\pi m^*}\right)AR \tag{8}$$

In Eqs. (7) and (8),  $X^*(t^*)$  and  $Y^*(t^*)$  are the instantaneous coordinates of the center of cylinder measured from the origin of the inertial frame of reference (Fig. 1).  $\ddot{X}^* = \frac{d^2 X^*}{dt^{*2}}$  and

$\dot{X}^* = \frac{dX^*}{dt^*}$ , respectively denote the normalized acceleration and velocity of the body along the streamwise direction while  $\ddot{Y}^* = \frac{d^2 Y^*}{dt^{*2}}$  and  $\dot{Y}^* = \frac{dY^*}{dt^*}$

represent the same quantities for cross-flow motion.  $C_d(t^*)$  and  $C_l(t^*)$ , respectively are the instantaneous flow-induced drag and lift coefficients of the body per unit length.

Equations (1) and (2) constitute an initial boundary value problem that is solved for fluid medium in a rectangular computational domain. Free-stream

inlet, stress-free or zero-traction exit, free slip on lateral boundaries and no-slip cylinder surface define the boundary conditions used for the problem. The no-slip condition for this moving boundary problem is time-dependent and hence needs reconstruction at each time step. A divergence-free velocity field is used as the initial condition to start the unsteady computations. Absence of an explicit equation for pressure eliminates the requirements of initial and boundary conditions on pressure. Equations (7) and (8) which are uncoupled or independent, form an initial value problem. At the start of computation for the lowest  $Re$ , the cylinder is released from rest at the origin, i.e.,  $X^*(0) = 0, \dot{X}^* = 0$  and  $Y^*(0) = 0, \dot{Y}^* = 0$ . However, for other  $Re$  values,  $X^*(0) = X_0^*, \dot{X}^* = \dot{X}_0^*$  and  $Y^*(0) = Y_0^*, \dot{Y}^* = \dot{Y}_0^*$ . Therefore, the initial conditions for flow and oscillator at the lowest  $Re$  correspond to release of the cylinder from rest at the origin in a fluid, the motion of which is started impulsively.

### 2.2 Space-Time Finite-Element Formulation

Two widely used approaches for handling moving boundary problems numerically (e.g., FVM, FEM) are the (1) Arbitrary Lagrangian Eulerian (ALE) formulation (Hughes *et al.* 1981; Dettmer and Peric 2006) and (2) Space-time formulation (Shakib, 1989; Shakib and Hughes, 1991; Tezduyar *et al.*, 1992 a,b; Perrochet and Azerat, 1995; Guler *et al.*, 1999). The ALE formulation takes into account the Lagrangian (mesh moves with fluid) as well as Eulerian (mesh fixed in space) methods simultaneously such that the mesh movement in ALE is independent of fluid motion. The mesh movement follows the movement of interface and entanglement of grid lines can be avoided. In the space-time method the variational formulation of the governing equations is extended over a space-time domain so that deformation of the spatial domain is determined automatically. To account for domain deformation, the shape or interpolation functions are considered to vary with space as well as time. While the spatial variation of shape function is continuous (e.g., piecewise bilinear), these are temporally discontinuous (piecewise constant or piecewise linear; see Eq. (11)). For a non-deforming domain, the trial solution for streamwise velocity component is represented in terms of time-independent shape functions  $N_i$  such that

$$u(x, y, t) = \sum_{i=1}^{N_n} N_i(x, y) U_i(t). \tag{9}$$

For space-time formulation, Eq. (9) is modified (see Donea and Huerta 2003) as

$$u(x, y, t) = \sum_{i=1}^{N_p} N_i(x, y) [\psi_1(t) u_i^n(t) + \psi_2(t) u_i^{n+1}(t)], \tag{10}$$

where,  $N_p$  and  $n$  stand for number of nodes per element and index for time level, respectively. The linear time interpolation functions  $\psi_1(t)$  and  $\psi_2(t)$  are defined as

$$\psi_1(t) = \frac{t^{n+1} - t}{t^{n+1} - t^n} \text{ and } \psi_2(t) = \frac{t - t^n}{t^{n+1} - t^n}. \tag{11}$$

The space-time domain is composed of several space-time slabs and time discontinuity enables one to locally solve for individual space-time slabs (Donea and Huerta 2003). The space-time finite-element formulation of Tezduyar *et al.* (1992 a, b) in conjunction with GLS (Galerkin Least Squares) stabilization is used for the present computations. Equal order of bilinear interpolation is used for the primitive variables (velocity and pressure). The interpolation functions ( $N_i$ , where  $i=1-4$ ) are bilinear in space and as seen from Eq. (11), linear in time ( $\psi_1$  and  $\psi_2$ ). With collocated arrangement of primitive variables, the number of (flow) unknowns per element in a space-time slab equals 4 (nodes per element) x 3 (nodal DOFs) x 2 (number of element layers in a slab) = 24.

### 2.3 Problem Statement and Mesh

The elastically mounted rigid elliptic cylinder resides in a rectangular computational domain such that the larger of its axes is oriented normal to the incoming stream (Fig. 1). Following the definition of  $AR$  presented in the inset of Fig. 1, this configuration of ellipse corresponds to  $AR > 1$ . The present computations are performed for  $AR = 1.11$ . The value of mass ratio of the cylinder is 1. The Cartesian coordinate system is stationary (inertial frame of reference) and displacements  $X$  and  $Y$  are measured relative to the origin of this coordinate system. A blockage of 5% corresponding to width of the computational domain =  $20D$ , is used. Also,  $L_u = 10D$  and  $L_d = 25.5D$  are used. The Reynolds number is based on the cross-stream projection ( $D$ ) of the cylinder and free-stream speed. A non-dimensional time step size of  $0.0625D$  is used for all the computations.

$U^*$  and  $F_N$  are fundamental non-dimensional input parameters. The free-stream speed is normalized with  $f_N$  and  $D$  such that  $U^* = U/(f_N D)$ . Following the definition of  $F_N$  in 2.1,  $U^*$  is the reciprocal of  $F_N$ . In the current numerical set-up,  $F_N$  is coupled to  $Re$ . The stationary vortex-shedding frequency at  $Re = 100$  is chosen as the reference natural frequency and  $F_N$  at any other  $Re$  scales inversely with this reference  $F_N$ . This constraint leads to the  $F_N = 16.91/Re$  relationship where 0.1691 is the vortex-shedding frequency (Strouhal number ( $St$ )) of a stationary elliptic cylinder of  $AR = 1.11$  at  $Re = 100$ . Therefore, the precise number 16.91 is the product of the reference  $F_N$  and reference  $Re$ . This kind of set-up has been used earlier for a circle by Willden and Graham (2006), Prasanth and Mittal (2008), Bahmani and Akbari (2010) and for a square by Sen and Mittal (2011). In the present work,  $U^*$  varies between  $50/16.91 = 2.96$  and  $180/16.91 = 10.64$ , where 50 and 180 are the lower and upper bounds of  $Re$ .

A block-structured non-uniform mesh consisting of 7437 nodes and 7236 bilinear quadrilateral elements is used for domain discretization. The number of nodes on the cylinder surface equals 104. The computational mesh is shown in Fig. 2a where a cross (x) indicates the fixed (0,0) position of the inertial frame of reference. Five constituent blocks

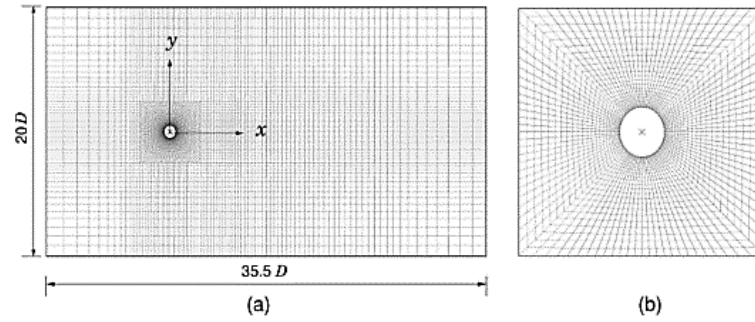


**Fig. 2. Structured, multi-block and non-uniform finite-element mesh employed for computing via a space-time method, free vibrations of a thick elliptic cylinder. The mesh consists of 7437 nodes and 7236 bilinear quadrilateral elements. The mesh corresponds to its undeformed configuration. Figure (b) shows the central block as well as the origin of the reference frame (marked via ×).**

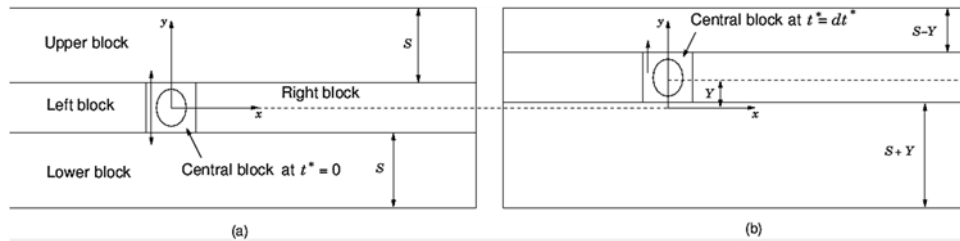


**Fig. 3. Schematic presentation of the remeshing scheme in terms of  $Y$ -only motion of cylinder: (a) undeformed configuration of the domain at  $t^* = 0$  and (b) deformation of upper and lower blocks at  $t^* = dt^*$ .**

are used to generate the mesh - a central square block (Fig. 2b) and four surrounding rectangular blocks, one each along the left, right, upper and lower directions (Fig. 3a). The central block contains the cylinder and executes identical rigid body translation as performed by the cylinder. The implementation of space-time formulation requires reconstruction of the mesh at each time step based on updated coordinates of every node in the mesh (see Sub-section 2.5) except for the four corners of the outer rectangular boundary of the domain.

### 2.4 Fluid-Solid Coupling

In VIV, the motion of the fluid and solid media is intrinsically coupled by the dynamic no-slip condition ( $u = \dot{X}, v = \dot{Y}$ ) as well as vortex-induced forces ( $C_d$  and  $C_l$ ), both at fluid-solid interface. The no-slip condition at the interface is updated based on the solution of Eqs. (7) and (8) for cylinder displacement. The displacement solutions are, in turn, functions of fluid loading that are computed from the flow obtained via solution of Eqs. (1) and (2). This interdependency defines the fluid-solid coupling. In the partitioned approach followed in the current study, within the same time slab, the global flow matrix (due to implicit time discretization) is solved by GMRES iterative solver while the space-time discretized rigid body equations are solved by numerical integration after reducing them to a system of first order ordinary differential equations in time.

The instantaneous fluid loading at the moving interface is computed by summing up the elementwise contributions of surface traction from all elements located at the fluid-solid interface. The

sectional force coefficients are thus computed from

$$(C_d, C_l) = \frac{1}{\frac{1}{2} \rho U^2 D} \int_{(\Gamma_t)_{interface}} (n \cdot \sigma)_{x,y} d\Gamma_t \quad (12)$$

where,  $(\Gamma_t)_{interface}$  denotes the FSI boundary of the domain  $\Omega_t$ , i.e. internal boundary or fluid-solid interface and  $\mathbf{n}$  is the unit normal to this boundary.

For this moving boundary problem, feedback between the flow system and oscillator unit obeys the following steps in succession: solution of the instantaneous flow field in conjunction with initial and boundary conditions (Eqs. (1) and (2)) – computations for instantaneous fluid loading (Eq (12)) – solution of ODEs for rigid body motion (Eqs. (7) and (8)); computation of the displacement of cylinder center from fixed inertial frame of reference – determination of updated position of cylinder center – remeshing (computing of updated nodal coordinates) – update of the specified velocity boundary conditions on the cylinder – repetition of the above steps at each time step.

### 2.5 Remeshing

The rectangular boundary of the computational domain as well as the reference frame remain stationary at all time instants. The use of a block-structured mesh over the computational domain aids in convenient remeshing at each time step. The remeshing scheme can be explained by considering the transverse-only motion (for example) of the cylinder as illustrated in Fig. 3. The first space-time slab is temporally bounded by the time interval

**Table 1 Unsteady flow past a stationary circular cylinder at  $Re = 100$ : comparison of the computed integral parameters with those available in the literature**

Author	Method	Blockage	$\bar{C}_d$	$C_{lmax}$	$C_{lrms}$	$St$
Williamson (1989)	Experiments	-	-	-	-	0.1648
Lin and Wu (1994)	Finite-volume	0.05	-	0.3467	0.2500	0.1619
Liu <i>et al.</i> (1998)	Finite-difference	-	1.3500	-	0.2500	0.1640
Singh and Mittal (2005)	Finite-element	0.05	1.3500	-	0.2500	0.1660
Posdziech and Grundmann (2007)	Spectral-element	0.025	1.3504	0.3309	-	0.1667
Jaiman <i>et al.</i> (2015)	Finite-element	0.05	1.3704	0.3374	0.2383	0.1683
Present	Finite-element	0.05	1.3887	0.3556	0.2518	0.1667

**Table 2 Flow past a stationary elliptic cylinder of aspect ratio 0.1 at  $45^\circ$  incidence: comparison of various integral parameters obtained from the present and earlier numerical studies at  $Re = 200$**

Author	Method	$\bar{C}_d$	$C_{lrms}$	$St$
Lugt and Haussling (1974)	Semi-analytical	1.4650	0.8925	0.2400
Chou (1992)	Finite-difference	1.3800	1.0900	0.2590
Present	Finite-element	1.3674	1.0473	0.2332

$[0, dt^*]$ . Considering upward travel of the cylinder over the time interval, Figs. 3a and 3b, respectively show the spatial domains  $\Omega_0$  and  $\Omega_{dt}$  at the limits of the interval. The absence of  $X$ -motion does not alter the size and shape of (does not deform) the left and right blocks. The instantaneous response  $Y(t)$  in Fig. 3b), shrinks the upper and expands the lower block to widths  $(S - Y)$  and  $(S + Y)$ , respectively where  $S$  is the unreformed width. The four neighbour blocks are constructed by non-uniformly spaced Cartesian grid lines. Therefore, deformation of the upper and lower blocks by a certain degree causes upward/downward translation of the horizontal grid lines. The vertical grid lines do not travel while they shorten or elongate. The mesh generator employs the algebraic method and requires information on the size of individual blocks and number of nodes and elements therein. The motion preserves the total (or blockwise) number of nodes and elements in the mesh as well as connectivity of the elements. The mesh generator is, therefore, provided with the required data for each component block at each time step and hence generates a new mesh without producing much projection error.

**2.6 Validation and Convergence Tests**

Comparison of the predicted integral parameters (mean drag ( $\bar{C}_d$ ), maximum lift ( $C_{lmax}$ ), r.m.s. lift ( $C_{lrms}$ ) and  $St$ ) with other results available from the literature for a stationary circular cylinder at  $Re = 100$  is presented in Table 1. The predicted integral parameters are in close agreement (maximum deviation of about 2.8% is seen for  $\bar{C}_d$ ) with those reported by the earlier efforts. A difference of 7.46% in predicted r.m.s. lift with those obtained by Posdziech and Grundmann (2007) is attributed to difference in blockage.

Extensive validation of stationary elliptical cylinder

results by us for steady flow can be found in Sen *et al.* (2012). Table 2 compares the predicted integral parameters for unsteady flow at  $Re = 200$  past a thin elliptic cylinder (stationary) of  $AR = 0.1$  at  $45^\circ$  incidence with those reported by Lugt and Haussling (1974) and Chou (1992). The definitions of drag and lift employed by Lugt and Haussling (1974) (Eqs. (10) and (14), respectively of their paper), involve an amplification factor of 2. The results reported by Lugt and Haussling (1974) for  $AR = 0.1$  and  $Re = 200$  in Figs. 12 and 15 of their paper are averaged to find the mean drag and lift. For each quantity, the last column of Figs. 12 and 15 are averaged leading to mean drag =  $\frac{2.97/2+2.89/2}{2} = 1.465$ , mean lift =  $\frac{1.82/2+1.75/2}{2} = 0.8925$  and mean Strouhal number =  $\frac{0.23+0.25}{2} = 0.24$ . The current predictions for  $\bar{C}_d$  and time-averaged lift ( $\bar{C}_l$ ) coefficients compare favourably (maximum difference  $\approx 4\%$ ) with those

obtained by Chou (1992). However, a difference of  $\approx 11\%$  is seen for  $St$ . Table 2 indicates that  $\bar{C}_d$  and  $\bar{C}_l$  of an  $AR = 0.1$  stationary elliptic cylinder at  $45^\circ$  incidence is, respectively overpredicted and underpredicted by Lugt and Haussling (1974) at  $Re = 200$ . For identical values of incidence angle and  $Re$  as above, Patel (1981) reported significant discrepancies with the results predicted by Lugt and Haussling (1974) for  $AR = 0.2$ . The value of  $\bar{C}_l$  reported by Lugt and Haussling (1974) is significantly smaller and  $\bar{C}_d$  significantly higher than the values obtained by Patel (1981) (see Fig. 15 of Patel 1981).

Lugt and Haussling (1974) employed a semi-analytical approach for handling the streamfunction-vorticity equations. Their grid involved  $75 \times 60$  nodes along the radial and circumferential directions. In addition, distance of the exit boundary from the center of the cylinder was eleven times the length of

**Table 3 Mesh convergence test for undamped  $Y$ -only VIV of a rigid ellipse of  $m^* = 1$  at  $Re = 70$**

Mesh	Nodes	Elements	$Y_{max}/D$	$\tilde{C}_d$	$C_{lrms}$	$St$
M1	7437	7236	0.5878	2.4539	0.5444	0.1866
M2	14780	14504	0.5892	2.4497	0.5481	0.1882

**Table 4 Test for adequacy of time step size on undamped  $Y$ -only VIV of a rigid ellipse of  $m^* = 1$  at  $Re = 70$**

$dt^*$	$Y_{max}/D$	$\tilde{C}_d$	$C_{lrms}$	$St$
0.0625	0.5878	2.4539	0.5444	0.1866
0.03125	0.6182	2.4471	0.5437	0.1871

the cylinder. In contrast, approximately doubled mesh resolution and extended computational domain are used for the current set of finite-element computations (refer to Section 2.3). It therefore appears that a coarse mesh coupled with lesser nodes on the cylinder and shorter domain size employed by Lugt and Haussling (1974) contribute to overprediction of drag and underprediction of lift.

Tests for mesh convergence, sufficiency of streamwise domain length components and adequacy of time step size can be found in Sen (2010) and Navrose *et al.* (2014) for  $m^* = 10$ . For completeness of the current computations, a mesh convergence study has been performed that establishes the adequacy of the mesh M1 containing 7437 nodes and 7236 bilinear quadrilateral elements to accurately predict the flow and VIV for  $m^* = 1$ . To this end, the undamped  $Y$ -only VIV at  $Re = 70$  is compared in Table 3 as computed using meshes M1 and M2 of roughly 1:2 resolution ratio. Table 4 ascertains the sufficiency of  $dt^* = 0.0625$  for the current computations.

### 3. RESULTS

Results for VIV of a thick elliptic cylinder of  $AR = 1.11$  and  $m^* = 1$  are presented for three different cases: (i) undamped transverse-only motion, (ii) damped transverse-only motion with  $\zeta = 0.044$  and (iii) undamped 2-DOF motion. Depending on the initial condition, solution multiplicity exists for problems involving moving boundaries. For VIV at low  $Re$ , these multiple solutions are generally captured close to the lock-in boundaries and often manifest in the form of hysteresis loops. To resolve the hysteresis or solution multiplicity in a numerical framework, progressive forward as well as backward computations are performed. Solutions at lower  $Re$  (or  $U^*$ ) are used for forward or 'increasing  $Re$ ' computations whereas for backward or 'decreasing  $Re$ ' computations, initial conditions are chosen from the higher  $Re$  (or  $U^*$ ) end.

For oscillators having low  $m^*$ , the response varies smoothly with  $Re$  in regions immediately next to the occurrence of resonance. It poses difficulty in identifying from the response curve, the exact  $Re$

marking the initial  $\rightarrow$  lower branch transition. However, existence of a prominent kink denoting this trend change could be identified in the oscillation frequency. The  $Re$  corresponding to the kink has been used in the present study to locate the transition  $Re$ .

#### 3.1 Undamped $Y$ -Only Motion Overview of the Cylinder Response Possible Explanation for Spike

The response is composed of the initial excitation and lower branches followed by decoherence (Fig. 4a). The constancy of slope of  $St$  or  $Y$  with  $Re$  (Fig. 4e) beyond  $Re = 65$  suggests that the lower branch initiates at  $Re = 65$ . The lock-in sets in at  $Re = 53$  and continues up to  $Re = 156$ . Along the forward path, the cylinder motion is mostly periodic with single dominant frequency except for  $Re = 155$  and  $156$  where flow is QP. For QP flow, the fluid forces and body motion contain multiple frequencies (Figs. 4f and 4g). At the extremities of lock-in, a single dominant shedding frequency prevails and a third harmonic coexists in the intermediate regime. This single- and multiple frequency behaviour of flow is obvious from the periodic  $C_l$ - $Y$  Lissajou plots in the insets of Fig. 4a. Primary hysteresis near the onset of resonance is absent. However, secondary hysteresis at the upper boundary exists only at a single  $Re$  of 154. At this  $Re$ , a solitary spike appears for backward computations. The authors are not aware of the existence of such spikes in response or fluid loading results in the VIV literature on bluff cylinders. Existence of the spike has been confirmed further via computations of the  $Re = 154$  (decreasing) flow using different initial conditions.

Near the closure of lock-in, the flow is periodic up to  $Re = 157$  (from higher- $Re$  end) and quasi-periodic for  $Re = 154 - 156$  (decreasing). Periodicity is recovered at  $Re = 153$  (decreasing) and maintained thereafter. The  $C_l$ - $Y$  Lissajou diagrams in Figs. 5a-5e demonstrate the periodicity  $\rightarrow$  quasi-periodicity  $\rightarrow$  periodicity transition. The spike at  $Re = 154$  might be an outcome of periodic flow/body motion along forward path (Fig. 4f) and quasi-periodic flow/body motion along reverse path (Fig. 4g). The consistency of this finding is further established via lift (Fig. 5f)

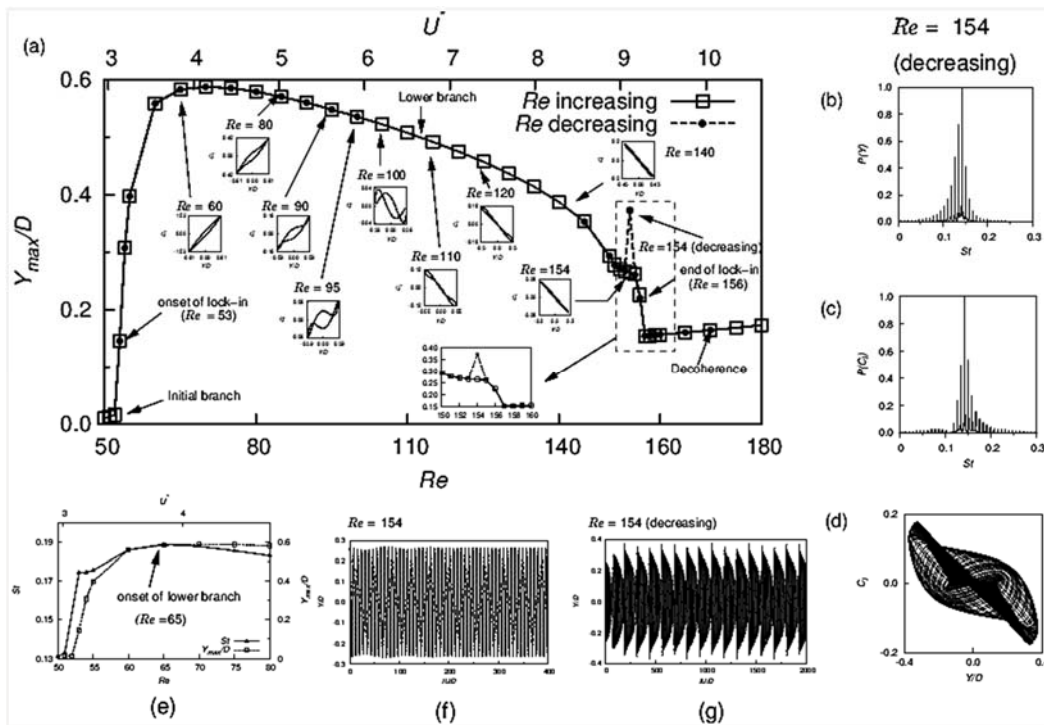


**Fig. 4.**  $Y$ -only undamped VIV of a rigid elliptic cylinder of  $m^* = 1$  and  $AR = 1.11$  for  $50 \leq Re \leq 180$  and 5% blockage: (a) variation of maximum transverse response,  $Y_{max}/D$  with  $Re$  and  $U^*$ , (b, c) power spectra of response and lift signals at  $Re = 154$  (decreasing), respectively, (d)  $C_l$ - $Y$  phase plot at  $Re = 154$  (decreasing), (e) close-up of  $Y$ - $Re$  and  $St$ - $Re$  curves near onset of lock-in, (f) periodic time-series of  $Y$  displacement at  $Re = 154$  and (g) quasi-periodic time-series of  $Y$  displacement at  $Re = 154$  (decreasing).

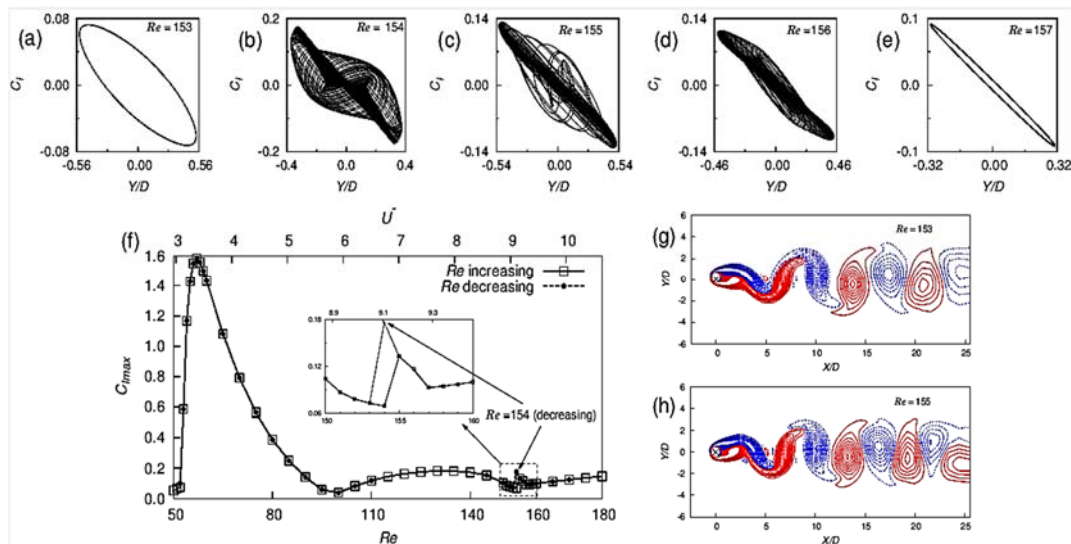


**Fig. 5.** Undamped  $Y$ -only motion of a thick elliptic cylinder: (a-e)  $C_l$ - $Y$  phase plots for  $Re = 153 - 157$  along the path of decreasing  $Re$ , (f)  $C_l$ - $Re$  curve showing the presence of a solitary spike at  $Re = 154$  (decreasing) and (g-h) instantaneous vorticity at  $Re = 153$  (decreasing) and  $155$  (decreasing).

which also shows a distinct spike at the same  $Re$ . Since Eq. (8) defines the  $C_l$ - $Y$  coupling, the  $Y$  curve also reflects the key features of  $C_l$ . In the neighbourhood of this spike, for reverse computations, the wake mode may be 2S or C(2S) even for comparable response. This is apparent from

Figs. 5g and 5h for showing 2S at  $Re = 153$  (decreasing) and C(2S) at  $Re = 155$  (decreasing) where the flow is periodic and QP, respectively. From here it also follows that the mode is 2S at  $Re = 154$  and C(2S) at  $Re = 154$  (decreasing) (Figs. 6c and 6d).

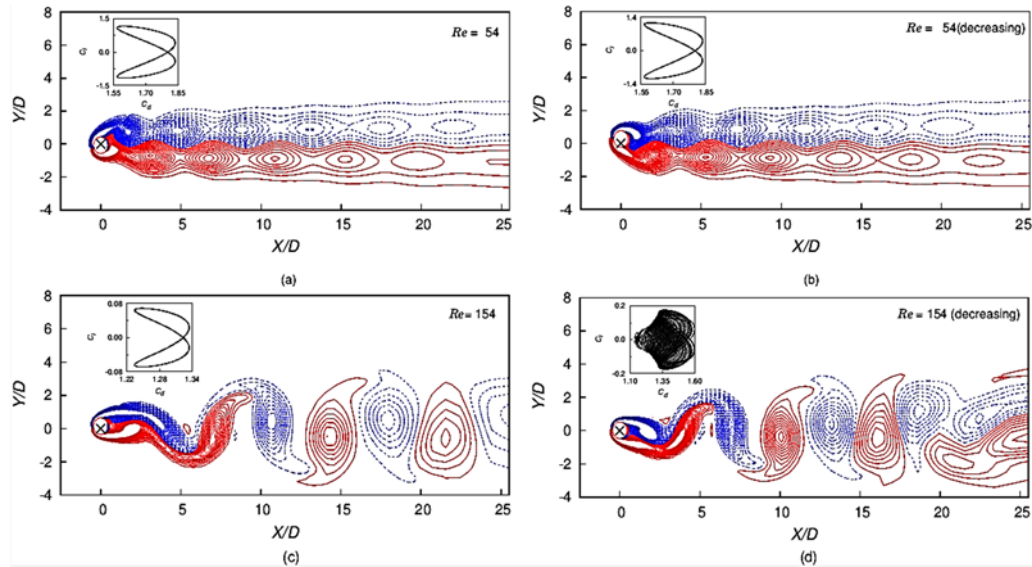


**Fig. 6. Undamped Y-only VIV of a rigid elliptic cylinder of  $m^* = 1$  and  $AR = 1.11$ : instantaneous vorticity at  $Re =$  (a) 54 and (b) 54 (decreasing). For both cases, the flow is periodic, the wake mode is  $C_{NW}(2S)$  and  $Y_{max}/D = 0.3074$ . For  $Re = 154$  (Fig. c), the flow is periodic, wake mode is 2S and  $Y_{max}/D = 0.2647$ . For  $Re = 154$  (decreasing) (Fig. d), the flow is quasi-periodic, wake mode is C(2S) and  $Y_{max}/D = 0.3733$ .**

### 1.1 Synchronization and Phase Shift

As is well known, the oscillation and vortex-shedding frequencies of a body collapse (1:1 synchronization) as long as it executes pure VIV. In consistency with this, the cylinder exhibits 1:1 synchronization for the range of  $Re$  considered. The normalized power spectra of transverse response (Fig. 4b) and lift (Fig. 4c) at  $Re = 154$  (decreasing) exhibit multiple peaks (QP flow/body motion) such that the value of the frequency ( $St = 0.1429$ ) corresponding to the dominant peak is identical (1:1 synchronization) from both FFTs. The multiple non-overlapping curves in the  $C_l$ - $Y$  Lissajou plot (Fig. 4d) confirms the QP nature of flow and body motion. The phase plot dominantly resides in the second and fourth quadrants implying that the transverse quantities are out of phase. The insets in Fig. 4a suggest that phase shift for undamped Y-only motion occurs between  $Re = 95$  and 100. For  $m^* = 10$  and  $AR = 1.11$ , Navrose *et al.* (2014) found that phase shift between  $C_l$  and  $Y$  for 2-DOF undamped VIV takes place in the vicinity of  $Re = 100$ . Presence of three loops in certain  $C_l$ - $Y$  phase portraits of Fig. 4a ensures the existence of a third harmonic in lift.

### Periodic, Quasi-Periodic Flows, Wake Modes

To further explore the periodic and quasi-periodic regimes of flow, the  $C_d$ - $C_l$  phase portraits at representative  $Re$  are shown in the insets of Fig. 6. The phase diagrams for  $Re = 54$  (Fig. 6a), 54 (decreasing) (Fig. 6b) and 154 (Fig. 6c) are closed, double-looped and contain a single crossover point located on zero lift axis. The figure eight kind of shape ensures periodicity of flow. The periodicity is characterized by oscillation frequency of  $C_d$  being twice the one of  $C_l$ . For  $Re = 154$  (decreasing) (Fig.

6d), the figure eight shape for subsequent cycles traverses between the extremities of fluid loading, the values of which vary with time. This is characteristic to QP flow. For the entire range of  $Re$ , the mean lift is zero (each crossover point resides on the zero lift axis) irrespective of flow being periodic or QP. Thus, the wake vortex mode must be one like 2S, C(2S) or 2P that form out of symmetric shedding from upper and lower rear halves of the cylinder. A non-zero  $\bar{C}_l$  results from asymmetric pressure distribution between the upper and lower surfaces of the cylinder. This unbalanced pressure leads to non-vanishing  $\bar{C}_l$  and hence, due to biased vortex-shedding, an asymmetric wake mode of vortex-formation, such as P+S, in the cylinder wake. It is possible to have unsymmetric wake mode even in 1:1 synchronization. The 1:1 synchronization implies that the time period of shedding and oscillation cycles is same. Thus, in the context of current study, two vortices of equal strength are alternately released per shedding cycle and contribute to the wake vortex mode. Hence, the wake mode must be 2S or its variant C(2S) for large response or  $C_{NW}(2S)$  for periodic initial branch.

In Fig. 6 showing selected wake modes, the initial position of the cylinder or the origin of the coordinate system is marked by a cross ( $\times$ ) symbol. The wake mode at  $Re = 54$  (increasing and decreasing) in the initial branch is  $C_{NW}(2S)$  as apparent from Figs. 6a and 6b, respectively. Figure 6c shows the 2S mode at  $Re = 154$  and Fig. 6d the C(2S) mode at  $Re = 154$  (decreasing). For the 2S mode,  $Y_{max}/D = 0.2647$  and when the normalized response reaches 0.3733, the mode changes to C(2S). The higher value of transverse response for the latter implies larger time period of oscillation or vortex-shedding cycle. Thus, the shed vortices get sufficient time to interact

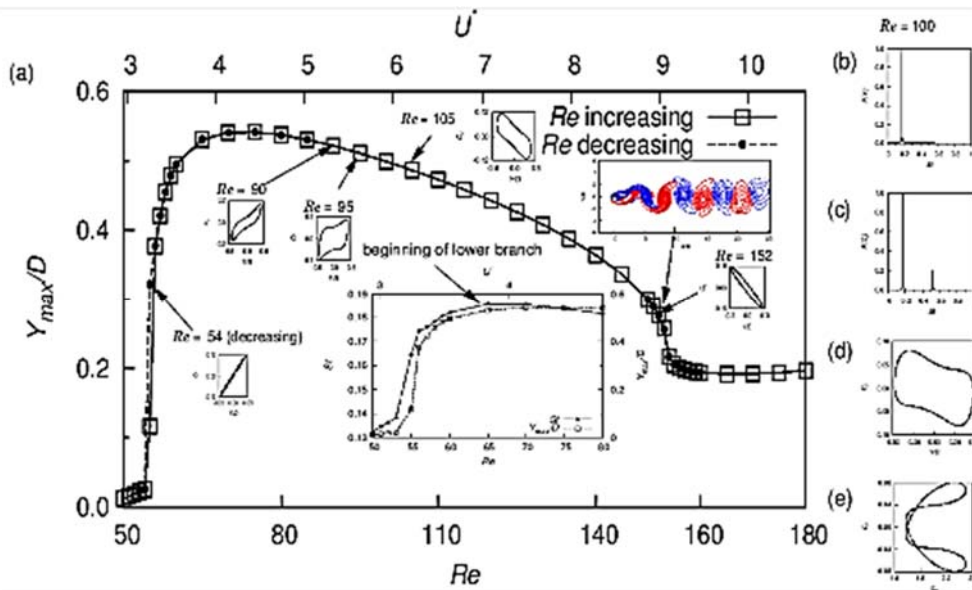


**Fig. 7. Damped ( $\zeta = 0.044$ ) Y-only VIV of a rigid elliptic cylinder of  $m^* = 1$  and  $AR = 1.11$  for  $50 \leq Re \leq 180$  and 5% blockage: (a) variation of maximum transverse response with  $Re$  and  $U^*$ . At  $Re = 100$ , figs. (b, c) show power spectra of response and lift while (d, e) show  $C_L$ - $Y$  and  $C_D$ - $C_L$  phase plots.**

**Table 5 Free vibrations of a rigid elliptic cylinder of  $m^* = 1$  and  $AR = 1.11$ : summary of the peak transverse response at the onset of lock-in and also over the entire range of  $Re$  considered. Also presented is a summary of hysteretic and non-hysteretic solutions**

	Y-only, $\zeta = 0$		X-Y-motion, $\zeta = 0.044$		X-Y motion, $\zeta = 0$	
	Onset of lock-in	Overall	Onset of lock-in	Overall	Onset of lock-in	Overall
$Y_{max}/D$	0.1459	0.5878	0.1167	0.5417	0.1415	0.6704
$Re$	53	70	55	75	53	80
$U^* = Re/16.91$	3.13	4.14	3.25	4.44	3.13	4.73
Hysteresis						
Primary	Absent		Very weak		Absent	
Secondary	Very weak		Absent		Strong	

among themselves and vortices from behind catch up those already shed. This might be a possible explanation on formation of C(2S) mode for large amplitude oscillations. The 2P mode corresponds to 1:2 type even sub-harmonic synchronization and hence any possibility of its presence for the current set of controlling parameters ( $Re = 50-180$ ) may be ruled out.

### 3.2 Damped Y-Only Motion

The effect of structural damping ( $\zeta = 0.044$ ) on the transverse response can be realized from the displacement curve presented in Fig. 7a. The introduction of damping is found to eliminate non-periodicity and a grossly periodic flow ( $C_L$ - $Y$  insets of Fig. 7a and Figs. 7d) with single oscillation frequency prevails over the entire regime of  $Re$  or  $U^*$ . While no appreciable impact is apparent on the range of synchronization, the peak value of response

indeed decays; a fall from  $0.5878D$  at  $Re = 70$  with  $\zeta = 0$  to  $0.5417D$  at  $Re = 75$  with  $\zeta = 0.044$  is observed (Table 5). The  $Re$  marking onset of lower branch, however, remains fixed at 65 as seen from the inset for  $St$ . The most interesting observation, however, relates to the hysteresis behaviour. The presence of damping eliminates quasi-periodicity as well as secondary hysteresis in the body response. This is perhaps the first reporting of a non-hysteretic response close to the upper extremity of lock-in for a vibrating body having smooth contours. However, solutions along forward and backward calculations diverge at  $Re = 55$  leading to very weak primary hysteresis. The regimes of hysteresis at the junctions of initial-lower branch and lower branch-decoherence involve periodicity or quasi-periodicity in flow (Fig. 4 of Navrose *et al.* 2014). We therefore conclude that the existence of hysteresis does not depend on the periodicity/quasi-periodicity of flow

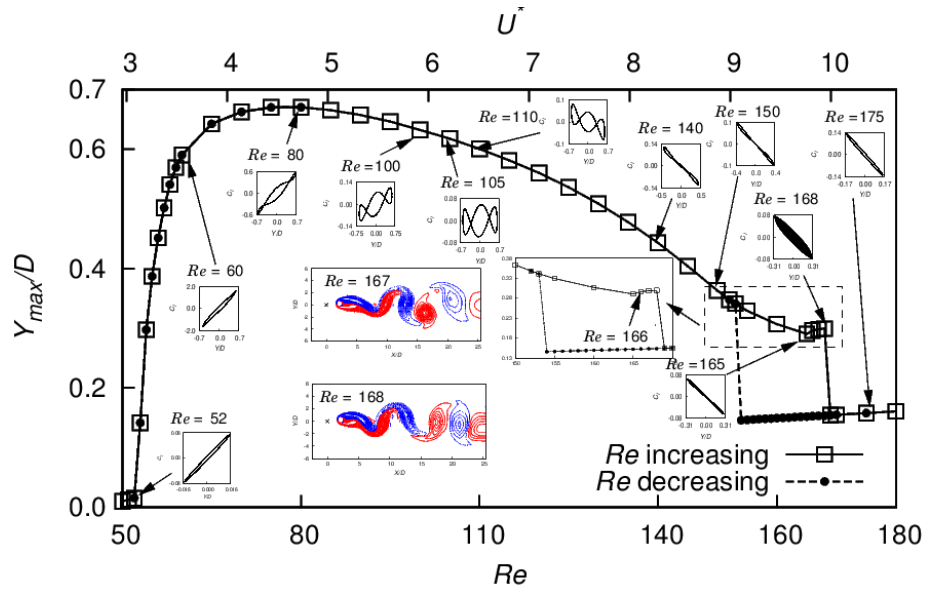


Fig. 8. VIV of a rigid elliptic cylinder of  $m^* = 1$  and  $AR = 1.11$  for  $50 \leq Re \leq 180$  and 5% blockage: variation of maximum transverse response with  $Re$  and  $U^*$  for  $X$ - $Y$ -motion.

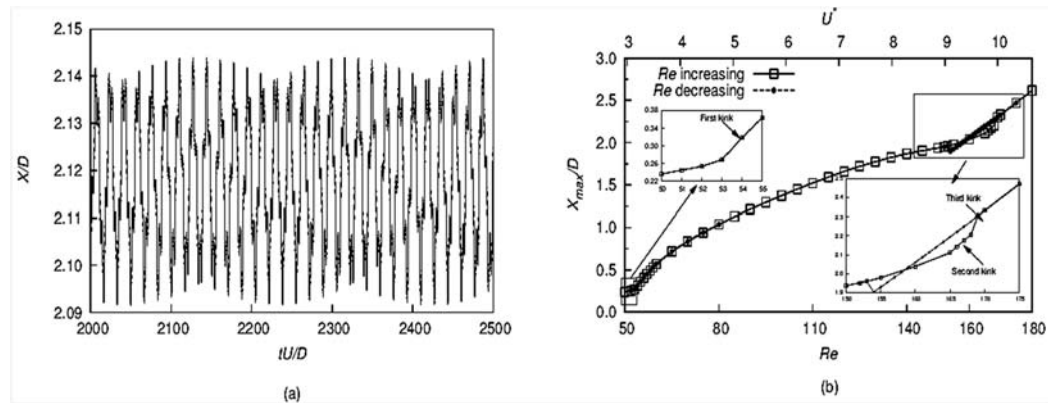


Fig. 9. Simultaneous undamped VIV with  $X$ - $Y$ -motion of a rigid ellipse of  $m^* = 1$  and  $AR = 1.11$  for  $50 \leq Re \leq 180$  and 5% blockage: (a) time trace of  $X$  at  $Re = 166$  and (b) variation of  $X_{max}/D$  with  $Re$  and  $U^*$ .

or damped /undamped nature of VIV. Interestingly the  $C_l$ - $Y$  phase diagrams are essentially single looped even in the presence of the third harmonic of  $St$  (Fig. 7d for  $Re = 100$ ).

### 3.3 Undamped $X$ - $Y$ -Motion

#### Overview of the Cylinder Response

Similar to the  $Y$ -only cases discussed in 3.1 and 3.2, the response is composed of initial and lower branches followed by a regime of decoherence. The flow is mostly periodic. Fig. 8a plots the transverse response with  $Re$  and  $U^*$ . Among the three cases considered, the magnitude of response and range of lock-in is maximum when the cylinder vibrates with an additional in-line DOF. The maximum value of  $Y$ -response,  $0.6703D$ , attained at  $Re = 80$ , is quite higher than the one ( $\approx 0.6D$ ) reported by Prasanth (2009) near the fundamental synchronization of an undamped circular cylinder of comparable  $m^*$  and identical flow conditions. Hysteresis is strong towards the upper limit of resonance whereas it

completely disappears at low  $Re$ . Decoherence sets in at  $Re = 169$ . The instantaneous vorticity at representative  $Re$  of 167 and 168 are shown in the insets of Fig. 8. The mode is 2S for both cases.

The in-line motion results from drag on the cylinder. Since drag is positive throughout, the in-line motion is executed only over  $x > 0$  region of the domain. Similar to  $\bar{C}_d$ , the magnitude of time-mean  $X$ -response is always positive. Fig. 9a showing the time trace of  $X$ -response at a representative  $Re$  of 166 illustrates this. Fig. 9b depicts the relationship between the maximum  $X$ -response and  $Re$  (or  $U^*$ ). The  $X$ -response in general, is found to increase with  $Re$ . Three kinks marking the onset of lock-in, onset of QP and start of decoherence are identified in  $X_{max}$  curve. Since  $X$  is measured from the fixed origin and mean  $X \neq 0$ , the  $X_{max}$  is not a real indicator of in-line displacement of the cylinder. In contrast, r.m.s. of the response is independent of the location of measurement reference and hence, the r.m.s. of in-

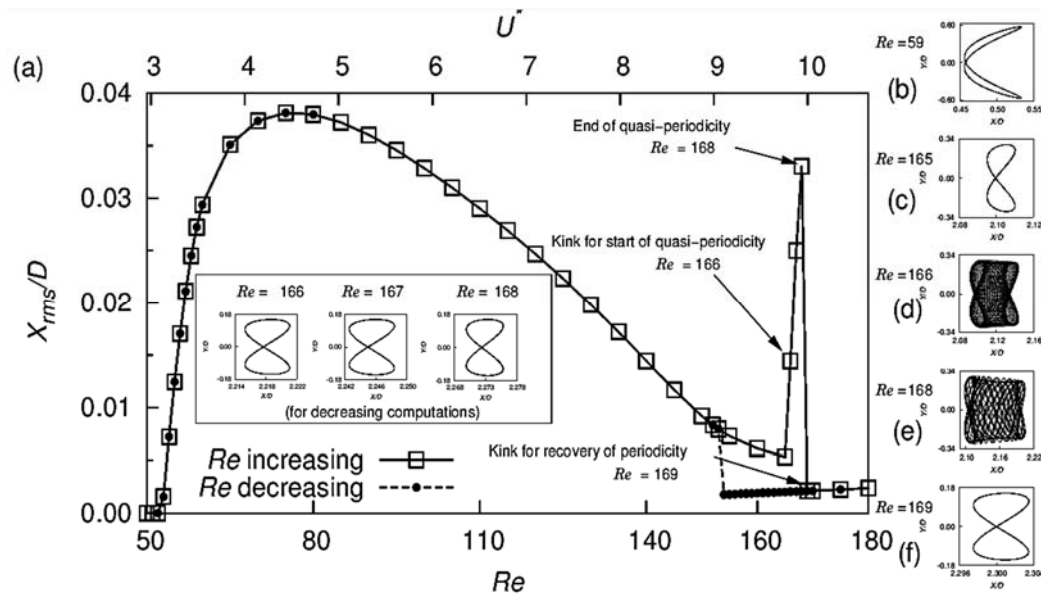


**Fig. 10. Simultaneous undamped VIV with  $X$ - $Y$ -motion of a rigid elliptic cylinder of  $m^* = 1$  and  $AR = 1.11$  for  $50 \leq Re \leq 180$  and 5% blockage: (a) root mean square of  $X$ -response plotted against  $Re$  and  $U^*$  and trajectory of the cylinder center for  $Re =$  (b) 59, (c) 165, (d) 166, (e) 168 and (f) 169.**

line response ( $X_{rms}$ ) is a better indicator of streamwise response. Fig. 10a plots the r.m.s. of  $X$ -response. A sharp spike is identified at  $Re = 168$ . A change of slope of  $X$  (or of  $Y$  in Fig. 8) at  $Re = 166$  marks the onset of QP regime. This continues till  $Re = 168$ . In this regime, the oscillation amplitude increases in either direction. The decoherence initiates at  $Re = 169$  and marks recovery of periodicity. We conclude that the spike in  $X_{rms}$  denotes the terminal point of lower branch. At this point,  $Y_{max}$  does not undergo any sharp variation (Fig. 8). It therefore appears that  $X_{rms}$  can more effectively indicate the end of synchronization when QP is associated with a spike.

### Flow Periodicity and Wake Modes

For  $Re = 59, 165, 166, 168$  and  $169$  covering the resonance branches, trajectory of the center of the cylinder is shown in Figs. 10b-10f via  $X$ - $Y$  phase plots. It is found that the flow/body motion is periodic for the initial and vast majority of lower branch. For  $Re = 166$  and  $168$ , the flow is quasi-periodic (Figs. 10d and 10e). However,  $Y$ -response for the same set of  $Re$  along the reverse path is insignificant and trajectories of figure eight shape ensure periodic flow/body motion (inset of Fig. 10a). An interesting observation from  $X$ - $Y$  phase plots in Fig. 10b-10f is that unlike the mean in-line response, transverse response is zero for each phase plot. This happens when the mean lift disappears. For such cases, vortex-shedding is symmetric, i.e., 2S or C(2S).

### Coupling Between $X$ - and $Y$ -Motion

Mathematically, the  $X$ - and  $Y$ -motion are decoupled. This is obvious from the rigid body Eqs. (7) and (8). The current computations for small mass ratio of unity demonstrate that  $X$ -response is significant and

it enhances the  $Y$ -response (compare Figs. 4a and 8a and also see Jauvtis and Williamson 2004).

### 3.4 Comparison of Response

At the onset of lock-in, the values of peak transverse response for all three cases of VIV are listed in Table 5. Irrespective of the DOFs of the cylinder, synchronization for undamped VIV initiates invariably at  $Re = 53$  or  $U^* = 3.13$ . The values of response are also comparable. For damped VIV, lock-in gets delayed with associated decay in the value of  $Y_{max}$ . Table 5 also compares the magnitudes of peak transverse response. Addition of damping and  $X$ -motion increases the value of  $Re$  or  $U^*$  associated with the maximum value of  $Y_{max}$ . A summary of the hysteresis behaviour at the lock-in boundaries presented in Table 5 indicates that no solution is fully hysteresis-free. As opposed to fully periodic flow/body motion for damped  $Y$ -only VIV, a narrow regime of quasi-periodicity towards the closure of lock-in exists for undamped VIV. Quasi-periodicity for  $Y$ -only VIV exists along the forward and backward paths whereas for  $X$ - $Y$ -motion, it is seen only along 'increasing  $Re$ '. For all three cases, initial to lower branch transition occurs at  $Re = 65$ . The  $St$  is found to attain its local maximum at this transition  $Re$ .

In consistency with the findings of Jauvtis and Williamson (2004), the undamped VIV results of  $m^* = 1$  cylinder with  $Y$ -only and  $X$ - $Y$ -motion differ significantly. An enhancement of maximum  $Y$ -response by 14% results from inclusion of  $X$ -motion to  $Y$ -only motion (see columns 2 and 6 of Table 5). Besides this, the range of lock-in widens. This is quite obvious from Fig. 11. With  $Y$ -only motion, the range of lock-in stretches from  $Re = 53$  to  $Re = 156$ . Addition of in-line DOF retains the lower limit to 53

**Table 6 Summary of the transitions in low  $Re$  VIV of a rigid elliptic cylinder of  $m^* = 1$  and  $AR = 1.11$**

VIV cases	QP near onset of lock-in	QP near end of lock-in	Number of kinks	Description of kinks
$Y$ -only, $\zeta = 0$	Absent	Weak, for increasing and decreasing $Re$	3	First kink at $Re = 53$ marking onset of lock-in, Second kink at $Re = 156$ for end of lock-in, Third kink at $Re = 158$ near decoherence
$Y$ -only, $\zeta = 0.044$	Absent	Absent	2	First kink at $Re = 55$ marking onset of lock-in, Second kink at $Re = 154$ for end of lock-in
$X$ - $Y$ , $\zeta = 0$	Absent	Weak, only for increasing $Re$	3	First kink at $Re = 53$ marking onset of lock-in, Second kink at $Re = 166$ for onset of quasi-periodicity, Third kink at $Re = 169$ for beginning of decoherence and recovery of periodicity

while shifts the upper limit further to 168. Finally, extent of secondary hysteresis with  $X$ - $Y$ -motion overwhelmingly exceeds its counterpart from  $Y$ -only motion.

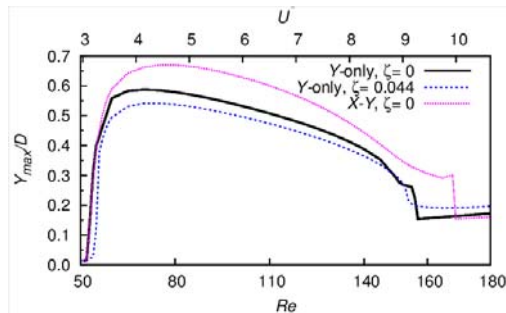


**Fig. 11. VIV of a rigid elliptic cylinder of  $m^* = 1$  and  $AR = 1.11$  for  $50 \leq Re \leq 180$  and 5% blockage: comparison of maximum transverse response for all three cases.**

### 3.5 Multiple Frequencies in Lift

For all the three cases, the periodicity of transverse response is associated with a single dominant frequency ( $St$ ). However, depending on  $Re$  (or  $U^*$ ), the periodicity of lift involves either a single frequency ( $St$ ) or a pair of frequencies including  $St$  and its third harmonic (also see Willden and Graham 2006 and Prasanth and Mittal 2008). The mono-frequency lift is observed close to the limits of lock-in whereas in the intermediate regime, the lift signal becomes periodic with two frequencies. Therefore, near the lock-in boundaries, the  $C_l$ - $Y$  phase portraits are single looped whereas three loops in general, can be identified in the rest of the periodic lower branch. However, an exception to the three loop profile with presence of  $St$  and  $3St$  is found for damped VIV.

The orientation of  $C_l$ - $Y$  phase plots provides an estimate of the phase angle between  $C_l$  (cause) and  $Y$  (effect). A phase plot located in the first and third quadrants implies an approximate in phase relationship between  $C_l$  and  $Y$ . A phase plot when resides in the second and fourth quadrants suggests a phase shift of about  $180^\circ$ . An exact in or out of phase

relationship requires the phase portrait to reduce to

$C_l = \pm Y/D$  line in phase plane. Figs. 4a and 7a suggest that the phase jump between  $C_l$  and  $Y$  for undamped and damped  $Y$ -only motion occurs for  $95 < Re < 100$ . The inclusion of in-line motion delays the phase jump to  $100 < Re < 110$ .

### 3.6 Identification of Transitions

A transition in VIV is reflected via trend change or presence of kinks in characteristic curves. For a freely vibrating square cylinder, Sen and Mittal (2016) showed that the number of transitions vary with  $m^*$ . Table 6 lists the number of kinks in  $Y$ -response and the associated  $Re$  marking their appearance. The onset of lock-in for low  $m^*$ , such as 1, does not necessarily mark the beginning of lower branch. The smoothness of the response curve for such low  $m^*$  poses difficulty in identifying the initial to lower branch transition. The actual number of kinks is determined from  $St$ - $Re$  curve. This number exceeds the one obtained from  $Y$ - $Re$  curve by one (for initial to lower transition).

## 4. CONCLUSIONS

Irrespective of the degree-of-freedom, an 1:1 synchronization between the transverse oscillation and vortex-shedding is observed for the entire range of  $Re$ . This suggests that the wake vortex mode must be a symmetric one with two vortices contributing to wake mode. The mode is 2S for low and C(2S) for high amplitude oscillations. It is  $C_{NW}(2S)$  in the periodic initial branch. The resistance due to structural damping lowers the overall displacement, shortens the range of lock-in while removing the quasi-periodicity and secondary hysteresis. Introduction of damping and additional in-line motion alters the upper limit of lock-in. The onset of lock-in, however, displays no appreciable sensitivity to these alterations. In general, the resonance begins in the neighbourhood of  $Re = 53$ . This study possibly for the first time, presents a unique response curve devoid of secondary hysteresis in bodies with smooth contours. This happens for damped  $Y$ -only motion. We conclude that presence of damping eliminates the non-periodic components that appear

at the lock-in boundaries. The time traces of response become pure sinusoids, i.e. periodic associated with single frequency. Addition of damping or translational DOF retains the basic branching behaviour of response; the response in each case is composed of initial and lower branches only. As opposed to high  $m^*$ , the onset of lock-in for low  $m^*$  does not necessarily coincide with the beginning of lower branch. A kink in oscillation frequency next to lock-in marks the transition from initial to lower branch. VIV of a low  $m^*$  ellipse with  $Y$ -only and  $X$ - $Y$ -motion differs considerably. The spike in  $X_{rms}$  signifies the upper limit of lower branch. For an undamped square cylinder, Sen and Mittal (2015, 2016) obtained complete hysteresis-free solutions for  $m^* = 1$ . In contrast, undamped VIV results of a circle by Prasanth and Mittal (2008) and Prasanth (2009) suggest that secondary hysteresis is always present. Further studies are needed to capture fully hysteresis-free solutions (if they exist) in a freely vibrating body with curved contours.

## REFERENCES

- Bahmani, M. H. and M. H. Akbari (2010). Effects of mass and damping ratios on VIV of a circular cylinder. *Ocean Engineering* 37, 511 - 519.
- Chou, M. H. (1992). An efficient scheme for unsteady flow past an object with boundary conformal to a circle. *SIAM Journal of Scientific and Statistical Computing* 13, 860 - 873.
- Dettmer, W. and D. Peric (2006). A computational framework for fluid-rigid body interaction: finite element formulation and applications. *Computer Methods in Applied Mechanics and Engineering* 195, 1633 - 1666.
- Donea, J. and A. Huerta (2003). *Finite element methods for flow problems*. John Wiley & Sons Ltd., England.
- Franzini, G. R., A. L. C. Fajarra, J. R. Meneghini, I. Korkischko and R. Franciss (2009). Experimental investigation of vortex-induced vibration on rigid, smooth and inclined cylinders. *Journal of Fluids and Structures* 25, 742-750.
- Guler, I., M. Behr and T. E. Tezduyar (1999). Parallel finite element computation of free-surface flows. *Computational Mechanics* 23, 117-123.
- Hughes, T. J. R., W. K. Liu and T. K. Zimmermann (1981). Lagrangian-Eulerian finite element formulation for incompressible viscous flows. *Computer Methods in Applied Mechanics and Engineering* 29, 329 - 349.
- Jaiman, R. K., S. Sen and P. S. Gurugubelli (2015). A fully implicit combined field scheme for freely vibrating square cylinders with sharp and rounded corners. *Computers and Fluids* 112, 1-18.
- Jauvtis, N. and C. H. K. Williamson (2004). The effect of two degrees of freedom on vortex-induced vibration at low mass and damping. *Journal of Fluid Mechanics* 509, 23-62.
- Khalak, A. and C. H. K. Williamson (1996). Dynamics of a hydroelastic cylinder with very low mass and damping. *Journal of Fluids and Structures* 10, 455 - 472.
- Khalak, A. and C. H. K. Williamson (1999). Motions, forces and mode transitions in vortex-induced vibrations at low mass-damping. *Journal of Fluids and Structures* 13, 813-851.
- Lin, S. Y. and T. M. Wu (1994). Flow control simulations around a circular cylinder by a finite volume scheme. *Numerical Heat Transfer A* 26, 301-319.
- Liu, C., Zheng, X. and C. H. Sung (1998). Preconditioned multigrid methods for unsteady incompressible flows, *Journal of Computational Physics* 139, 35 - 57.
- Lugt, H. J. and H. J. Haussling (1974). Laminar flow past an abruptly accelerated elliptic cylinder at 45° incidence. *Journal of Fluid Mechanics* 65, 711-734.
- Navrose, Yogeswaran, V., S. Sen and S. Mittal (2014). Free vibrations of elliptic cylinders at low Reynolds numbers. *Journal of Fluids and Structures* 51, 55-67.
- Patel, V. A. (1981). Flow around the impulsively started elliptic cylinder at various angles of attack. *Computers and Fluids* 9(4), 435-462.
- Perrochet, P. and P. Azerat (1995). Space-time integrated least-squares: solving a pure advection equation with a pure diffusion operator. *Journal of computational Physics* 117, 183-193.
- Posdziech, O. and R. Grundmann (2007). A systematic approach to the numerical calculation of fundamental quantities of the two dimensional flow over a circular cylinder. *Journal of Fluids and Structures* 23, 479 - 499.
- Prasanth, T. K. (2009). *Vortex-induced vibration at low Reynolds numbers*. PhD thesis, Indian Institute of Technology Kanpur, India.
- Prasanth, T. K. and S. Mittal (2008). Effect of blockage on free vibration of a circular cylinder at low Re. *International Journal for Numerical Methods in Fluids* 58, 1063–1080.
- Sen, S. (2010). *Flow past stationary and vibrating cylinders of various cross-sections at low Reynolds numbers*. PhD thesis, Indian Institute of Technology Kanpur, India.
- Sen, S. and S. Mittal (2011). Free vibration of a square cylinder at low Reynolds numbers. *Journal of Fluids and Structures* 27, 875-884.
- Sen, S. and S. Mittal (2015). Effect of mass ratio on free vibrations of a square cylinder at low Reynolds numbers. *Journal of Fluids and Structures* 54, 661-678.
- Sen, S. and S. Mittal (2016). Free vibrations of a

- square cylinder of varying mass ratio. *Procedia Engineering* 144, 34-42.
- Sen, S., Mittal, S. and G. Biswas (2012). Steady separated flow past elliptic cylinders using a stabilized finite-element method. *Computer Modeling in Engineering and Sciences* 86, 1-28.
- Shakib, F. (1989). *Finite element analysis of the compressible Euler and Navier-Stokes equations*. PhD Thesis, Stanford University.
- Shakib, F. and T. J. R. Hughes (1991). A new finite element formulation for computational fluid dynamics: IX. Fourier analysis of Space-time Galerkin/least-squares algorithms. *Computer Methods in Applied Mechanics and Engineering* 87, 35-58.
- Singh, S. P. and S. Mittal (2005). Vortex-induced oscillations at low Reynolds numbers: Hysteresis and vortex-shedding modes. *Journal of Fluids and Structures* 20, 1085 - 1104.
- Sivakumar, P., R. P. Bharti and R. P. Chhabra (2007). Steady flow of power-law fluids across an unconfined elliptic cylinder. *Chemical Engineering Science* 62, 1682-1702.
- Tezduyar, T. E., M. Behr and J. Liou (1992a). A new strategy for finite element computations involving moving boundaries and interfaces-the DSD/ST procedure: I. The concept and the preliminary numerical tests. *Computer Methods in Applied Mechanics and Engineering* 94, 339-351.
- Tezduyar, T. E., M. Behr and J. Liou (1992b). A new strategy for finite element computations involving moving boundaries and interfaces-the DSD/ST procedure: II. Computation of free-surface flows, two-liquid flows, and flows with drifting cylinders. *Computer Methods in Applied Mechanics and Engineering* 94, 353-371.
- Willden, R. H. J. and J. M. R. Graham (2006). Three distinct response regimes for the transverse vortex-induced vibrations of circular cylinders at low Reynolds numbers. *Journal of Fluids and Structures* 22, 885-895.
- Williamson, C. H. K. (1989). Oblique and parallel modes of vortex shedding in the wake of a circular cylinder at low Reynolds numbers. *Journal of Fluid Mechanics* 206, 579-627.